Geometric Swimming at Low and High Reynolds Numbers

Ross L. Hatton, *Member, IEEE,* Howie Choset, *Member, IEEE,*

Abstract—**Several efforts have recently been made to relate the displacement of swimming three-link systems over strokes to geometric quantities of the strokes. In doing so, they provide powerful, intuitive representations of the bounds on a system's locomotion capabilities and the forms of its optimal strokes or gaits. While this approach has been successful for finding net *rotations*, noncommutativity concerns have prevented it from working for net *translations*. Our recent results on other locomoting systems have shown that the degree of this noncommutativity is dependent on the coordinates used to describe the problem, and that it can be greatly mitigated by an optimal choice of coordinates. Here, we extend the benefits of this optimal-coordinate approach to the analysis of swimming at the extremes of low and high Reynolds numbers.**

Index Terms—**locomotion, swimming, geometric mechanics, coordinate choice, Lie brackets.**

I. INTRODUCTION

SWIMMING has received attention in fields ranging from robotics to fluid mechanics to biology. The physics of self-propulsion through a surrounding fluid have long driven new results in these areas and led to insightful observations regarding the behavior of swimming organisms [1], [2], [3]; in robotics these observations serve as guides for the design and control of micro-swimmers and novel aquatic systems [4], [5]. A particularly interesting observation is that the swimming motions that optimally convert joint motion into net displacement are essentially the same for systems at both low and high Reynolds numbers, even though the fluid forces are dominated by viscous drag at low Reynolds numbers and by inertial accelerations at high Reynolds numbers [6].

Historically, swimming dynamics have been investigated by applying a stroke pattern (taken from nature or intuition) to a model of the swimming system and then analyzing the resulting forces and displacements. More recently, the strokes themselves have been the focus of attention, with optimal patterns found at low [7] and high [8] Reynolds numbers. Whilst these optimizations have primarily been achieved by parameterizing a stroke primitive and then applying standard optimization techniques find the parameters which give the best performance, a second research thrust has applied curvature techniques based on Lie brackets to differential geometric formulations of the system models to directly find useful strokes [6], [9], [10], [5], [11], [12]. These curvature approaches successfully capture the net displacements resulting

from small-amplitude strokes, but due to noncommutativity,[1] provide only the net rotations and coarse approximation of the net translations resulting from finite changes in shape.

The development of the geometric models for swimming has been paralleled by the development of similar models in robotics for nonholonomically constrained systems [13], [14], [15], [16], [17]; this line of research has included similar Lie bracket approaches to those developed in the swimming community. The parallel developments are unsurprising, as both branches of inquiry are based on the same underlying body of theory, with roots in [18].

Working within the context of nonholonomic mechanics, we have recently developed a set of mathematical tools for manipulating the geometric models. The first of these, the connection vector field [19], provides a visual representation of the kinematics of locomoting systems. Our second development, optimized coordinate choice [20], [21], reduces the noncommutativity of the systems and expands the benefit of the Lie bracket techniques, providing close approximations of the net translations over finite strokes.

The primary goal of this paper is to demonstrate the applicability of these tools, particularly the coordinate optimization process, to swimming systems at low and high Reynolds numbers; this purpose is achieved in §§3-5. In §6, we then use these tools to examine the phenomena underlying previous numerical results for optimized swimming. Preparatory to this analysis, we offer in §2 a brief review of the previously developed geometric swimming models. Our intention in presenting these models is to provide an intuitive understanding of their derivation to a reader familiar with vector calculus but not differential geometry; accordingly, we have limited the presence of geometric terminology in the text and moved it into the footnotes. It is our hope that these notes will serve as a starting point for the reader who wishes to dig deeper into the literature on the underlying mathematical structures.

An earlier version of this paper appeared in the proceedings of the ASME 2010 Dynamic Systems & Control Conference [22]. The present work includes an expanded discussion of the role of Lie brackets in defining the area integration rules and corrects an implementation error in optimizing the xy coordinates of the body frame. This correction enables considerably stronger claims in §VI as to the correspondence between stroke performance and features in the curvature plots.

R. L. Hatton is with the School of Mechanical, Industrial, and Manufacturing Engineering at Oregon State University. H. Choset is with the Robotics Institute at Carnegie Mellon University, Pittsburgh, PA. email: ross.hatton@oregonstate.edu

---

[1]The net displacement over a trajectory depends on the order of intermediate translations and rotations, and the curvature techniques discard all or some of this ordering information.

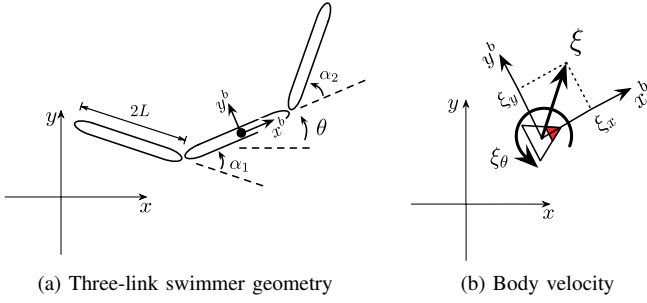(a) Three-link swimmer geometry (b) Body velocity

Fig. 1: Model coordinates

II. SYSTEM MODELS

In this paper, we analyze the motion of three-link systems of the form illustrated in Fig. 1(a), swimming at the extremes of low and high Reynolds numbers.[2]. This three-link model was proposed by Purcell [2] as the simplest system capable of swimming at low Reynolds numbers, and similar reasoning [9] suggests the use of this model for the high Reynolds number case. The motion of the swimmers as they interact with their surroundings is dictated by the *reconstruction equation*, which encodes constraint forces and momentum conservation rules as functions of the system shape and shape velocity. At both low and high Reynolds numbers, the reconstruction equation simplifies to a kinematic form, generated respectively from the drag forces on the swimmer or the net conservation of momentum between the swimmer and the surrounding fluid.

A. The Reconstruction Equation and the Local Connection

When analyzing a multi-body locomoting system, it is convenient to separate its configuration space Q (i.e., the space of its generalized coordinates q) into a position space G and a shape space M, such that the position $g \in G$ locates the system in the world, and the shape $r \in M$ gives the relative arrangements of its bodies.[3] For example, the position of the three-link system in Fig. 1(a) is the location and orientation of the middle link, $g = (x, y, \theta) \in SE(2)$,[4] and its shape is parameterized by the two joint angles, $r = (\alpha_1, \alpha_2)$.[5]

With this separation, locomotion is readily seen as the means by which changes in shape (such as strokes, gaits, or wingbeats) affect the position. Members of the geometric mechanics community[14], [15], [16], [17] have addressed this problem with the development of the *reconstruction equation* and the *local connection*, tools for relating the body velocity of the system, ξ, i.e., its longitudinal, lateral, and rotational velocity as depicted in Fig. 1(b), to its shape velocity $\dot{r}$, and accumulated momentum p.

[2]Low and high Reynolds number respectively identify fluid regimes dominated by viscosity and inertia. Micro-swimmers, to whom even water is high-viscosity, are typically modeled using low Reynolds number physics; the high Reynolds number model we use here is an idealization of the fluid flow around a meso- or macro-scale swimmer such as a fish.

[3]In the parlance of geometric mechanics, this assigns Q the structure of a (trivial, principle) *fiber bundle*, with G the *fiber space* and M the *base space*.

[4]SE(2) is the set of all translations and rotations in the plane.

[5]This model is adaptable to systems with continuous curvature by treating the shape parameters as the amplitudes of *curvature modes* [23].

The general reconstruction equation is of the form

$$\xi = -\mathbf{A}(r)\dot{r} + \mathbf{\Gamma}(r)p, \tag{1}$$

where $\mathbf{A}(r)$ is the *local connection*, a matrix which relates joint to body velocity, $\mathbf{\Gamma}(r)$ is the *momentum distribution function*, and p is the *generalized nonholonomic momentum*, which captures how much the system is "coasting" at any given time [15].

For systems that are sufficiently constrained or unconstrained, such as at the extremes of very low and very high Reynolds numbers, the generalized momentum drops out and the system behavior is dictated by the *kinematic reconstruction equation*,

$$\xi = -\mathbf{A}(r)\dot{r}, \tag{2}$$

in which the local connection thus acts as a kind of Jacobian, mapping from velocities in the shape space to the corresponding body velocity. For the rest of this paper, we will focus our attention on exploiting the structure of this kinematic reconstruction equation.

B. Low Reynolds Number Swimmer

At very low Reynolds numbers, viscous drag forces dominate the fluid dynamics of swimming and any inertial effects are immediately damped out.[6] This effect has two consequences, whose combination [6], [11] results in the equations of motion for this system taking on the form of a kinematic reconstruction equation as in (2). First, the drag forces on the swimmer are linear functions of the body and shape velocities. Second, the net drag forces and moments on an isolated system interacting with the surrounding fluid go to zero: if the swimmer were to move with any velocity other than that dictated by force equilibrium, the large viscous forces would almost instantaneously remove this "excess" velocity, returning the system to the equilibrium velocity.

For an illustration of the first consequence, consider a three-link swimmer with links modeled as slender members according to Cox theory [24]. For simplicity here, we regard the flows around each link as independent, per resistive force theory [7].[7] The drag forces and moments on the ith link are based on a principle of lateral drag coefficients being larger than those in the longitudinal direction [24], with a maximum ratio of $2:1$ in the limit of an infinitesimally thin member. The moment around the center of the link is found by taking the lateral drag forces as linearly distributed along the link according to its rotational velocity, i.e.,

$$F_{i,x} = \int_{-L}^{L} \frac{1}{2}k\xi_{i,x}d\ell = kL\xi_{i,x} \tag{3}$$

$$F_{i,y} = \int_{-L}^{L} k\xi_{i,y}d\ell = 2kL\xi_{i,y} \tag{4}$$

$$M_i = \int_{-L}^{L} k\ell(\ell\xi_{i,\theta})d\ell = \frac{2}{3}kL^3\xi_{i,\theta}, . \tag{5}$$

[6]This characterization of course assumes that there are no nearby objects to reflect momentum, etc.

[7]The solution for coupled flows is of the same form, but has additional shape-dependent terms in the forces on each link.

where $F_{i,x}$ and $F_{i,y}$ are respectively the longitudinal and lateral forces, M_i the moment, k the differential viscous drag constant, and $\xi_i = [\xi_{i,x}, \xi_{i,y}, \xi_{i,\theta}]^T$ is the body velocity of the center of the ith link.[8] The link body velocities are readily calculated from the system body and shape velocities as

$$\xi_1 = \begin{bmatrix} \cos(\alpha_1)\xi_x - \sin(\alpha_1)\xi_y + \sin(\alpha_1)L\xi_\theta \\ \sin(\alpha_1)\xi_x + \cos(\alpha_1)\xi_y - (\cos(\alpha_1) + 1)L\xi_\theta + L\dot{\alpha}_1 \\ \xi_\theta - \dot{\alpha}_1 \end{bmatrix} \tag{6}$$

$$\xi_2 = \xi \tag{7}$$

$$\xi_3 = \begin{bmatrix} \cos(\alpha_2)\xi_x + \sin(\alpha_2)\xi_y + \sin(\alpha_2)L\xi_\theta \\ -\sin(\alpha_2)\xi_x + \cos(\alpha_2)\xi_y + (\cos(\alpha_2) + 1)L\xi_\theta + L\dot{\alpha}_2 \\ \xi_\theta + \dot{\alpha}_2 \end{bmatrix}, \tag{8}$$

where the velocity of the second link is identified with the body velocity of the system, and all are clearly linear functions of ξ and $\dot{\alpha}$ and nonlinear functions of α. By extension, the forces in (3)–(5), which are linearly dependent on the link body velocities, are also linear functions of ξ and $\dot{\alpha}$ and nonlinear functions of α. Summing these forces into the net force and moment on the system (as measured in the system's body frame),

$$\begin{bmatrix} F_x \\ F_y \\ M \end{bmatrix} = \begin{bmatrix} \cos\alpha_1 & \sin\alpha_1 & 0 \\ -\sin\alpha_1 & \cos\alpha_1 & 0 \\ L\sin\alpha_1 & -L(1+\cos\alpha_1) & 1 \end{bmatrix} \begin{bmatrix} F_{1,x} \\ F_{1,y} \\ M_1 \end{bmatrix}$$
$$+ \begin{bmatrix} F_{2,x} \\ F_{2,y} \\ M_2 \end{bmatrix} + \begin{bmatrix} \cos\alpha_2 & -\sin\alpha_2 & 0 \\ \sin\alpha_2 & \cos\alpha_2 & 0 \\ L\sin\alpha_2 & L(1+\cos\alpha_2) & 1 \end{bmatrix} \begin{bmatrix} F_{3,x} \\ F_{3,y} \\ M_3 \end{bmatrix}, \tag{9}$$

preserves the linear relationship with the velocity terms while only adding further nonlinear dependence on α, such that the net forces $F = [F_x, F_y, M]^T$ can be expressed with respect to the velocities as

$$F = \omega(\alpha) \begin{bmatrix} \xi \\ \dot{\alpha} \end{bmatrix}, \tag{10}$$

where ω is a 3×5 matrix.

We now turn to the second consequence of being at low Reynolds number, that the net forces and moments on an isolated system should be zero, i.e., $F = [0,0,0]^T$. Applying this rule and separating ω into two sub-blocks gives

$$\begin{bmatrix} 0 \\ 0 \\ 0 \end{bmatrix} = \begin{bmatrix} \omega_1^{3\times3} & \omega_2^{3\times2} \end{bmatrix} \begin{bmatrix} \xi \\ \dot{\alpha} \end{bmatrix}, \tag{11}$$

and thus $\omega_1\xi = -\omega_2\dot{\alpha}$ and

$$\xi = -\omega_1^{-1}\omega_2\dot{\alpha}. \tag{12}$$

Finally, setting $\mathbf{A} = \omega_1^{-1}\omega_2$ into (12) into the form of (2), with the viscous drag forces thus generating the local connection for the low Reynolds number system. In the hydrodynamically coupled case, the viscous flows around the links that produce the drag forces in (3)–(5) additionally depend on the relative

positions and velocities of the links (i.e., the shape and shape velocity of the system), but retain the linear relationships with ξ and $\dot{\alpha}$ that produce (10) and its sequels [6].

C. High Reynolds Number Swimmer

At very large Reynolds numbers, viscous drag is negligible and inertial effects dominate the swimming dynamics. While these conditions appear to be the direct opposite of those in the low Reynolds number case, they also result in the system equations of motion forming a kinematic reconstruction equation.[9] This fact can be demonstrated via several approaches of varying technical depth [6], [9], [10], but to maximize the physical intuition associated with this derivation, we give here a novel presentation based on the Lagrangian approach for the planar skater used in [16], [17].

The heart of this approach is the recognition that for a system whose Lagrangian is equal to its kinetic energy (i.e., it has no means of storing potential energy), that is isolated from external forces (i.e., energy can only be added or removed from the system through generalized forces applied to the "internal" shape variables), and whose kinetic energy can be expressed as

$$KE = \frac{1}{2} \begin{bmatrix} \xi & \dot{r} \end{bmatrix} \mathbb{M}(r) \begin{bmatrix} \xi \\ \dot{r} \end{bmatrix}, \tag{13}$$

the mass matrix $\mathbb{M}$ contains within itself the local connection [17]. Specifically, $\mathbb{M}$ is of the form

$$\mathbb{M} = \begin{bmatrix} \mathbb{I}(r) & \mathbb{I}(r)\mathbf{A}(r) \\ (\mathbb{I}(r)\mathbf{A}(r))^T & m(r) \end{bmatrix}, \tag{14}$$

from which $\mathbf{A}$ is easily extracted.[10] If such a system starts at rest, the generalized momentum p in (1) remains zero for all time, and the system's equations of motion take the form of (2).

Given this formula for the local connection, it just remains to be shown that the three-link swimmer at high Reynolds number meets the afore-mentioned Lagrangian conditions. The first condition, that the Lagrangian equal the kinetic energy, can be easily seen by observing that for a planar system with no gravity effects in the plane, there is no mechanism for storing potential energy, leaving only the kinetic term in the Lagrangian. The second condition, that the system is isolated from external forces, follows from the lack of dissipative forces in the high Reynolds number regime. The third condition, on the form of the swimmer's kinetic energy, is more subtle, and as above, we will use a hydrodynamically decoupled example while noting the existence of an equivalent coupled solution.

---

[8]Note that by "body velocity", we mean the longitudinal, lateral, and rotational velocity of the link, and not its velocity with respect to the body frame of the system.

[9]Note that in this section, we follow the example of [9], [10] and neglect the contribution of vortex shedding to swimming. Models of swimming that do include vortex shedding can be found in works such as [25], [26], [8]

[10]In the works from which this derivation was inspired, $\mathbb{I}(r)$ appears as the *locked inertia tensor* of an articulated body on a frictionless plane (i.e., its mass and rotational inertia with its joints locked in a given position). In the present fluid example, $\mathbb{I}$ has a similar interpretation, except that its product with velocity produces the *Kelvin impulse* of the combined fluid/rigid system rather than the momentum [10]. The Kelvin impulse is a momentum-like quantity, measuring the impulse required to halt a moving system; its advantage here is that it allows for a fluid field of infinite extent (and hence infinite mass), for which momentum is an ill-defined quantity.

An object immersed in a fluid displaces this fluid as it moves. In an ideal inviscid fluid, the drag forces on the object are entirely due to this displacement, and act as directional *added masses* $\mathcal{M}$ on the object that sum with the actual inertia of the object to produce the effective inertia of the combined system. The added masses of single rigid bodies (and elements of articulated bodies when the inter-body fluid interactions are neglected) are solely functions of the geometries of the bodies. For example, the added mass tensor of an ellipse with semi-major axis a and semi-minor axis b in a fluid of density ρ is

$$\mathcal{M} = \begin{bmatrix} \mathcal{M}_x & 0 & 0 \\ 0 & \mathcal{M}_y & 0 \\ 0 & 0 & \mathcal{M}_\theta \end{bmatrix} = \begin{bmatrix} \rho\pi b^2 & 0 & 0 \\ 0 & \rho\pi a^2 & 0 \\ 0 & 0 & \rho(a^2-b^2)^2 \end{bmatrix},$$
(15)

with $\mathcal{M}_x$, $\mathcal{M}_y$, and $\mathcal{M}_\theta$ respectively corresponding to the added mass for longitudinal, lateral, and rotational motion.

Returning to the three-link swimmer, the kinetic energy associated with motion of the ith link through the fluid is

$$KE_i = \frac{1}{2}\xi_i^T(I_i + \mathcal{M}_i)\xi_i,$$
(16)

where I_i is the link's inertia tensor, $\mathcal{M}_i$ its added mass, and ξ_i is its body velocity, as calculated in (6)–(8). Using the same linear dependence of ξ_i on ξ and $\dot{r}$ as we exploited in the low Reynolds number case, it is relatively straightforward to transform (16), and thus $KE = \sum KE_i$, into the form of (13), and from there to extract the local connection $\mathbf{A}$. The derivation for the hydrodynamically coupled case is essentially similar, with the chief difference being the additional dependence of $\mathcal{M}$ on r, which captures the distortion of the flow around each link caused by the proximity of the other links [6].

D. Similarity to Nonholonomic Systems

While the swimming systems described above seem significantly different from the nonholonomically constrained systems we have examined in our previous work [27], there are some strong underlying similarities. The ω matrix for the low Reynolds number system in (11) acts as a *Pfaffian constraint* on the system, multiplying the body and shape velocities to produce a zero vector. This Pfaffian constraint form also appears in the case of systems with nonholonomic constraints, such as wheels that can roll but not slip sideways. In fact, with just two small changes, we can convert the low Reynolds number swimmer into the *three-link kinematic snake* [17], [20] which has a nonholonomic constraint (such as a passive wheelset) at the center of each link, preventing lateral motion but freely allowing longitudinal and rotational motion. First, concentrating the lateral force at the link center, rather than distributing it along the link, replaces (5) with $M_i = 0$ for each link, allowing free rotation. Second, increasing the lateral/longitudinal drag ratio from its value of 2 in (3) and (4) makes it increasingly difficult for the links to move sideways. In the limit that this ratio approaches ∞, these drag forces behave like the ideal nonholonomic constraints on the kinematic snake, preventing lateral motion while freely allowing longitudinal motion.
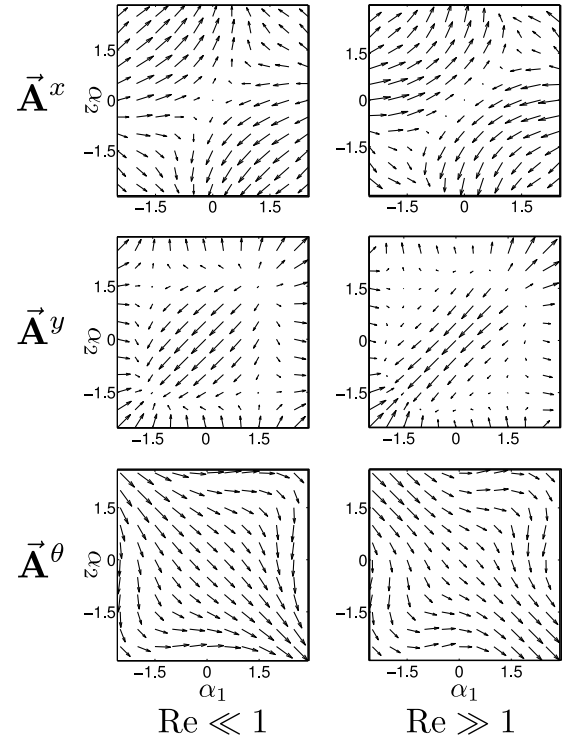

Fig. 2: Connection vector fields for the low and high Reynolds number swimmers.

Likewise, the high Reynolds number swimmer bears a strong resemblance to the *three-link floating snake* [14], [17], [19], which consists of three links resting on a frictionless plane. In this case, the parallel is even easier to draw, as the floating snake is simply a high Reynolds number swimmer in which the added mass in (16) goes to zero, leaving only the actual inertias of the links. An interesting difference between these two systems is that while the high Reynolds number swimmer can both translate and rotate, the floating snake can only rotate. This property highlights the importance of directionality in locomotion: the added mass on the swimmer is orientation-dependent, allowing it to push its leading surfaces forward at low inertia, then increase their inertia to draw in the tail, but the floating snake's mass is fixed, so pushing one segment forward always generates an equal and opposite reaction in the other segments.

III. CONNECTION VECTOR FIELDS

The expressions for $\mathbf{A}$ are somewhat complicated, and provide no particular insight as to the behavior of the system. Geometrically plotting them, however, does provide this insight and we have developed several tools for visualizing the local connection. The first of these tools is the *connection vector field* [19].

Each row of the local connection $\mathbf{A}(r)$ can be considered as defining a vector field $\vec{\mathbf{A}}^i$ on the shape space whose dot product with the shape velocity produces the corresponding component of the body velocity,

$$\xi_i = \vec{\mathbf{A}}^i(r) \cdot \dot{r}$$
(17)

where, for convenience, we wrap the negative sign into the vector field definition.[11] These connection vector fields encode the (local) gradients of the position variables with respect to the shape variables, highlighting how the position changes in response to a given shape change: A shape change that follows a connection vector field moves the system positively along the corresponding body direction, while one that is orthogonal to the field produces no motion in the corresponding body direction.

The connection vector fields for the (hydrodynamically decoupled) swimming models described above are shown in Fig. 2, with the low Reynolds model at the ideal infinitesimally thin limit and an aspect ratio of $a/b = 10$ for the elliptical links of the high Reynolds number model. The strong resemblance between the two sets of fields is immediately apparent, and underscores the physical similarities between the two systems: although the fluid forces on the links are viscous at low Reynolds numbers and inertial at high Reynolds numbers, they both resist lateral motion significantly more strongly than they do longitudinal motion, forcing the swimmers into trajectories that minimize lateral motion of their links.

We can also build physical intuition for the systems by observing the individual structures of the fields. For instance, both $\vec{\mathbf{A}}^\theta$ fields have a general heading in the $+\alpha_1, -\alpha_2$ direction. Returning to the geometry of the swimmer in Fig. 1(a), we see that this heading encodes a tendency for the center link to counter-rotate with respect to the outer links. Physically, this makes sense, as rotating an outer link towards the center link generates opposite reaction forces on the center link. Similar intuition applies to other features of the vector fields, such as how the $\vec{\mathbf{A}}^x$ and $\vec{\mathbf{A}}^y$ fields approach zero magnitude in the vicinity of $\alpha = (0,0)$ for $\vec{\mathbf{A}}^x$ and $\alpha = (\pm\pi/2, \pm\pi/2)$ for $\vec{\mathbf{A}}^y$: In these shapes the outer links are respectively aligned or perpendicular to the center link, and lateral reaction forces on them project into pure lateral or pure longitudinal forces on the center link.

IV. CONSTRAINT CURVATURE FUNCTIONS

Connection vector fields illustrate the instantaneous relationship between shape and position changes, but do not directly convey information about the *net* change in position over a sequence of shape motions. Knowledge about such net motion plays a key part in understanding and controlling their behavior, as the joint limits force the systems to use cyclic motions that include both forward and backward segments. The *curvature* of the local connection encodes useful information about this net displacement [18], which can be visually represented as a set of *constraint curvature functions* (CCFs) over the shape space [10], [11], which have also been referred to (for two-dimensional shape spaces) as *height functions* [17].

At an intuitive level, the CCFs are closely related to the curls of the rows of the local connection. By Green's form of Stokes' theorem [28], the line integral on a vector field along a closed loop is equal to the area integral of the field's curl over the interior of the loop. Plotting the curl of $\vec{\mathbf{A}}^\theta$ as a function on
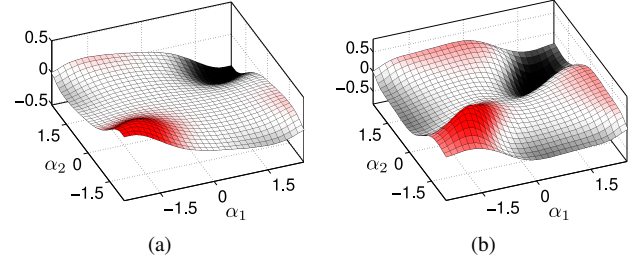

Fig. 3: θ Curls of the local connection for the (a) low and (b) high Reynolds number swimmers. Because the θ component of the Lie bracket is 0, these curls are also the θ CCFs for their respective sytems.

the shape space, as in Fig. 3, allows intuitive identification of cyclic strokes that produce desired net rotations: For positive net rotation (positive value of $\Delta\theta = \int \xi_\theta \, dt$), the most effective strokes are those that positively (counterlockwise) encircle regions of the shape space where $\text{curl}\vec{\mathbf{A}}^\theta > 0$ or negatively (clockwise) encircle regions where $\text{curl}\vec{\mathbf{A}}^\theta < 0$. Conversely, when zero net rotation is desired (such as when the system should move in a straight line over repeated iterations of a stroke), the stroke should encircle regions from the second or fourth quadrants, or explicitly balance negative and positive regions in its encirclements.

More precisely, the relationship between $\text{curl}\mathbf{A}^\theta$ and net rotation is a special case of an identity between the *exponential coordinates*[12] [10] $z(\phi)$ of the net displacement over a stroke ϕ (a closed trajectory in the shape space) and a series whose first two terms correspond to the integral of the abstract *curvature* of the constraints over a region of the shape space bounded by ϕ [29]. This curvature is measured by the *Lie bracket* of the local connection, which measures the net translation induced by a differential oscillation in the system's shape. For two shape dimensions, the identity appears as

$$z(\phi) = \iint_\phi \overbrace{-\text{curl}\mathbf{A}}^{\substack{\text{CCFs (full Lie bracket)}}} + \underbrace{\big[\mathbf{A}_1, \mathbf{A}_2\big]}_{\text{noncommutativity}} \, dr + \text{higher-order terms}, \quad (18)$$

$$\underbrace{\phantom{-\text{curl}\mathbf{A}}}_{\text{nonconservativity}}$$

where the curl operator is applied individually to each row of $\mathbf{A}$, and $[\mathbf{A}_1, \mathbf{A}_2]$ is the *local* Lie bracket of the columns of $\mathbf{A}$

---

[11]In strict differential geometric language, each row $\mathbf{A}^i$ of $\mathbf{A}$ is a one-form over M acting on $\dot{r}$, and $\vec{\mathbf{A}}^i$ is the negative dual of that one-form.

[12]The exponential coordinates of a position are the components of the constant body velocity required to reach that position in unit time, starting from the origin. A mapping between exponential coordinates and displacements is provided in [10], but for the purposes of this paper, it is sufficient to note that on $SE(2)$ this mapping is an identity mapping for pure translation, i.e., $\exp([z_x, z_y, 0]^T) = (z_x, z_y, 0)$, and in the θ component, i.e., $\exp([a, b, z_\theta]^T) = (c, d, z_\theta)$.

(taken as if **A** did not depend on the shape).[13,14] On $SE(2)$, this local Lie bracket evaluates as

$$\begin{bmatrix} \mathbf{A}_1, \mathbf{A}_2 \end{bmatrix} = \begin{bmatrix} \mathbf{A}_1^y \mathbf{A}_2^\theta - \mathbf{A}_2^y \mathbf{A}_1^\theta \\ \mathbf{A}_2^x \mathbf{A}_1^\theta - \mathbf{A}_1^x \mathbf{A}_2^\theta \\ 0 \end{bmatrix}. \qquad (19)$$

The integrand in (18) is the (negative) curvature of the local connection, whose components are the system CCFs in much the same way that the negative components of **A** form the connection vector fields. Within this curvature, the curl term measures the *nonconservativity* of the local connection, or how the constraints change over the shape space, preventing antipodal segments of a stroke from pushing or pulling the system equally. The local Lie bracket and higher order terms correspond to the *noncommutativity* of the system's position space, i.e., the extent to which translations with intermediate rotations do not commute, as in parallel parking maneuvers.

For motions over which a system experiences little non-commutativity, the higher-order terms are small and the net displacement is closely approximated by the area integral of the first two terms in the equation (the system's CCFs).[15] This makes it easy to characterize the locomotive capabilities of the system, in terms of the maximum displacement possible over any gait, and, as we discuss in the §VI, to design useful gaits by simply encircling appropriate regions of the shape space. Historically, this condition of low noncommutativity was considered as only applying to small-amplitude gaits or certain special cases [10]. In our recent work [21], [27], however, we have demonstrated a means for optimizing the coordinates to minimize the overall system noncommutativity and apply the CCF area rules to large-amplitude motion.

V. MINIMUM-PERTURBATION COORDINATES

An interesting property of (18) is that the noncommutativity captured in the higher-order terms does not directly scale with the magnitude of the input stroke ϕ. Instead, it scales with the intermediate rotations (and, to a lesser extent, translations) the system experiences as it executes the stroke. This is a subtle distinction—increasing the stroke amplitude in general increases the intermediate motion—and the noncommutative limitations on integrating displacement via the area rule were long viewed as limitations on the admissible stroke size [10]. In our work on nonholonomic systems, however, we observed that in many instances the noncommutativity can be alleviated by an appropriate choice of coordinates for the system's

---

[13]In general, a Lie bracket of two actions a and b identifies the difference between doing "a then b" and "b then a," which is equivalent to taking the action "a then b then the opposite of a then the opposite of b." For the swimmer, the full Lie bracket corresponds to assigning the actions as "increase α_1 and displace by $\mathbf{A}_1 \cdot d\alpha_1$" and "increase α_2 and displace by $\mathbf{A}_2 \cdot d\alpha_2$." The local connection is re-evaluated at each new shape in the cycle, and so the net displacement incorporates both changes in **A** and any noncommutativity in moving along $\mathbf{A}_1$ and $\mathbf{A}_2$. The *local* Lie bracket takes the actions as "displace by $\mathbf{A}_1 \cdot d\alpha_1$" and "displace by $\mathbf{A}_2 \cdot d\alpha_2$," and so misses any shape dependency of the local connection; these effects appear as the curl of **A**. Further discussion of this difference appears in [30].

[14]This identity generalizes to higher dimensions with flux-like integrals replacing the area integration, but here we restrict our attention to two shape variables.

[15]Rotational motion always commutes on $SE(2)$, producing the special case that net rotation is exactly equal to the area integral of the curl.

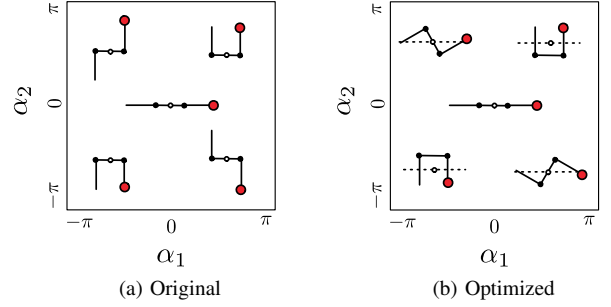(a) Original   (b) Optimized

Fig. 4: Configuration of the swimmer in the original and optimized coordinates.

body frame [20]. In these choices of coordinates, the body frame (i.e. the point we track on the system) rotates and translates very little as the swimmer moves in response to changes in shape, much as the center of mass of an isolated system remains stationary even if its individual components are moving over complex trajectories. Reducing this tracked motion (which does not alter the actual motion of the system) minimizes the noncommutative influence of the higher order terms.

As described in [21], [27], we find these *minimum-perturbation coordinates* by first defining the location of their corresponding body frame with respect to the original body frame as $\beta(r) = (\beta_x, \beta_y, \beta_\theta) \in SE(2)$. The gradients of β with respect to the shape give the relative velocity of the original and new body frames as the shape changes. Because the rotational velocity of the new frame is equal to that of the original frame plus the relative velocity, the rotational part of the new connection can be expressed as

$$\xi_\theta^{new} = -\mathbf{A}_{new}^\theta(r)\dot{r} = \left(-\mathbf{A}^\theta(r) + \nabla_r \beta_\theta(r) \right)\dot{r}. \qquad (20)$$

To minimize the observed rotational velocity for arbitrary shape velocities, averaged over a region Ω of the shape space, we solve for the $\beta_\theta(r)$ that minimizes the norm of this new connection row, i.e. minimizes an objective function D_θ for

$$D_\theta = \iint_\Omega \| -\mathbf{A}^\theta + \nabla_r \beta_\theta \|^2 \, d\Omega. \qquad (21)$$

This minimization corresponds to performing a *Hodge-Helmholtz decomposition* on $\mathbf{A}^\theta$, which can be solved via finite element methods as described in [31]. Minimizing translation of the new body frame follows a similar procedure, except that a cross-product term couples the optimal β_x and β_y to each other and to the original $\mathbf{A}^\theta$, so that the objective function becomes

$$D_{xy} = \iint_\Omega \| -\mathbf{A}^x + \nabla_r \beta_x - (-\mathbf{A}^\theta \beta_y) \|^2$$
$$+ \| -\mathbf{A}^y + \nabla_r \beta_y + (-\mathbf{A}^\theta \beta_x) \|^2 \, d\Omega. \qquad (22)$$

We present a finite element algorithm for solving this equation (which is the generalization of Hodge-Helmholtz decomposition to $SE(2)$) in [27].

The optimal choices of body frame for both three-link swimmers under this criterion are approximately the mean

orientation of the three individual links and the center of mass location, with small, shape-dependent weightings of the contribution of each link to the averages.[16] Figure 4 shows how these new coordinates affect our representation, with the swimmer shown in five shapes with orientation $\theta = 0$. Using the coordinates from Fig. 1(a), the center links of the swimmer are aligned across the different shapes, but in the new coordinates, the dotted lines representing the mean orientation are now aligned.

The connection vector fields and CCFs for the two swimmers in the optimized coordinates are shown in Figs. 5(a) and 5(b). These plots highlight several interesting features of the coordinate optimization process and the differences between the motions of the low and high Reynolds number swimmers. First, the CCFs for θ are unchanged in the new coordinates, even though their respective connection vector fields have clearly been modified. As explained in [21], θ is optimized by applying the Hodge-Helmholtz decomposition [32] to the original $\vec{\mathbf{A}}^{\theta}$ field to separate it into its gradient and rotational components; the gradient component encodes the relationship between the original and optimized measures of θ, and the rotational component is the new $\vec{\mathbf{A}}^{\theta}$. As the gradient component of a vector field by definition does not contribute to its curl, removing it from $\vec{\mathbf{A}}^{\theta}$ does not modify the associated CCF.

Second, symmetries in the motion of the swimmer are immediately apparent, suggesting locations for single-loop and figure-eight strokes that produce displacements in specific directions [17]. Third, the magnitudes of the connection vector fields and CCFs are significantly larger for the high Reynolds number swimmer. Going back to the derivations in §2, we observe that the ratio of lateral to longitudinal drag on the low Reynolds number swimmer is $2 : 1$, while the added masses at high Reynolds number are based on the $10 : 1$ aspect ratio of the links; we hypothesize that the high Reynolds number swimmer is thus able to gain a greater difference from "pushing" links longitudinally and "pulling" them laterally than is the low Reynolds number system, and thus achieve greater velocities and displacements over comparable strokes.

VI. ANALYSIS

Using the CCFs in optimized coordinates, we can now start to answer some previously posed questions about swimming, and to explain prior result about optimal strokes that had been reached only by numerically integrating the swimmers' motions over a wide array of candidate strokes.

A. Purcell's Swimmer

The three-link swimmer was introduced by E. M. Purcell as an example in his lecture "Life at Low Reynolds Numbers" [2]. He also assigned to it the simplest possible stroke, in which the joints move individually and sweep through equal positive and negative angles, and used symmetry arguments to
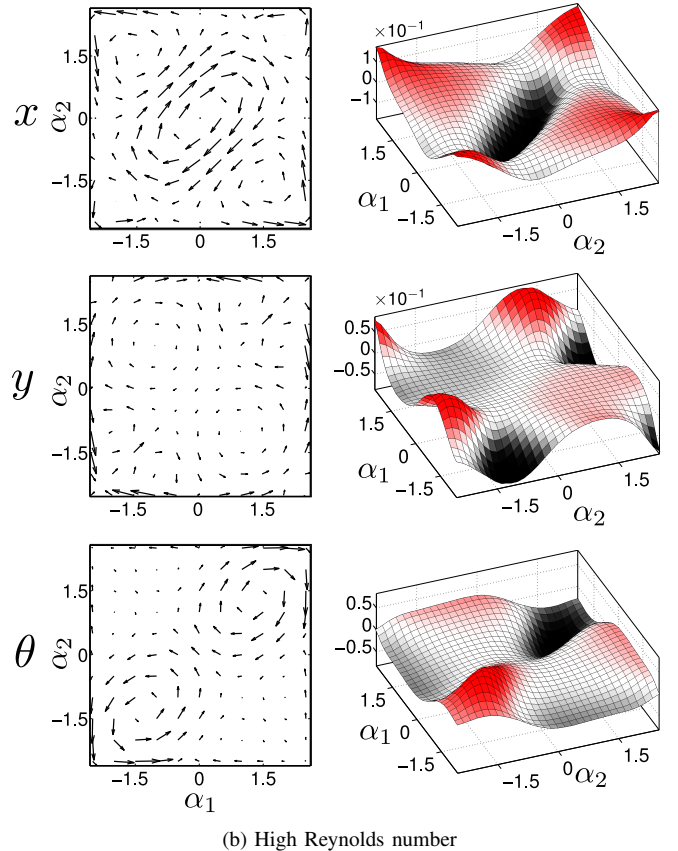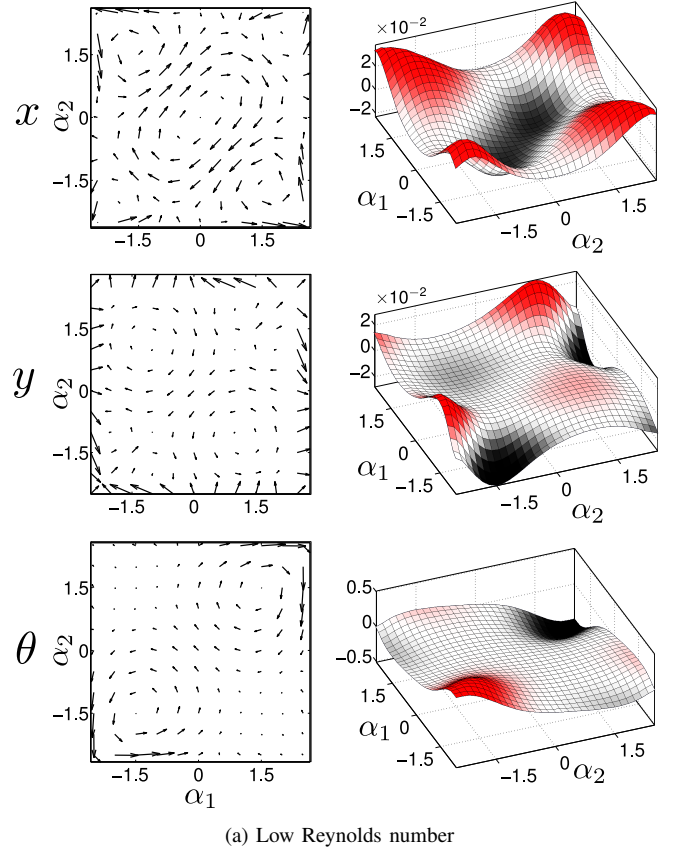
---

[16]Systems with different geometries (e.g. unequal link lengths) will of course have different minimum-perturbation coordinates, corresponding to their dynamics as expressed in the values of their **A** matrices.

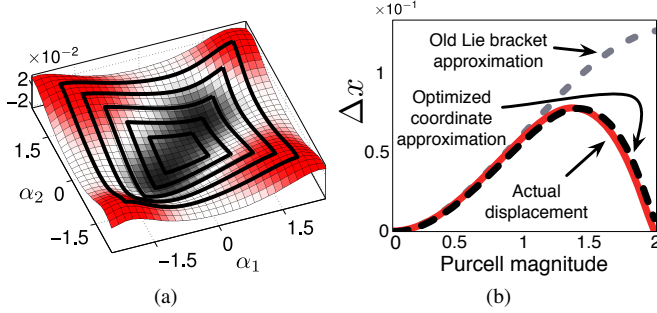(a) Low Reynolds number

(b) High Reynolds number

Fig. 5: Connection vector fields and CCFs in optimized coordinates.

Fig. 6: Purcell strokes (a) and resulting displacements (b). Scale is for a unit total swimmer length with equal link lengths.

Fig. 7: Approximate and actual displacements for the Purcell swimmer with a middle link that is (a) 1.5 the length of an outer link, as in [11], and (b) 0.75 the length of an outer link, as in [7]. Scale is for a unit total swimmer length.

show that the stroke moves the swimmer forward. More recently, Becker *et al.* [33] demonstrated that a sufficiently large-amplitude Purcell stroke moves the swimmer *backward*. Using the CCFs in minimum-perturbation coordinates, we can now extend the qualitative geometric explanation for this change in direction provided in [11] to a quantitative description that captures the amplitudes at which forward displacement ceases to increase and at which it becomes negative.

Purcell strokes trace out squares on the shape space as shown in Fig. 6(a). At small amplitudes, the x CCF is entirely negative in the region bounded by the square, so following the square clockwise produces a net positive displacement in the x direction (all the squares symmetrically enclose positive and negative regions of the y and θ CCFs, so we focus our attention on the x direction). As the amplitudes grow larger, they first expand the negative region they enclose, then start incorporating positive area, reducing the magnitude of displacement and eventually changing its sign. Figure 6(b) demonstrates that the approximation on which this CCF explanation rests is essentially exact for Purcell magnitudes up to at least 2 radians, predicting the net displacement with negligible error. By contrast, curvature predictions that used un-optimized coordinates (such as the similar analysis presented in [11]) diverge from the correct solution for gaits larger than 1 radian, and predicts a continued *increase* in positive net displacement at the magnitude where the true displacement passes through zero.

We should note that as the quality of the Lie bracket approximation is related to the magnitude of the connection vector fields, the swimmer's geometry (and thus its dynamics) affects how accurate the approximation is in the un-optimized coordinates. For example, Fig. 7 shows how the original and optimized Lie brackets agree with the net displacement for a swimmer with a middle link that is longer [11] or shorter [7] than the outer links. Comparing these plots with Fig. 6(b), the Lie bracket of the system considered in [11] (whose short arms propel the middle link less for a given change in joint angle, and thus induce naturally-smaller connection vector fields) provides a much better approximation of the optimal Purcell amplitude than in the equal-link-lengths case, but still does not capture the change in sign (direction) of the net motion. Conversely, un-optimized application of the Lie bracket to the long-armed system in [7] (which was determined to be the
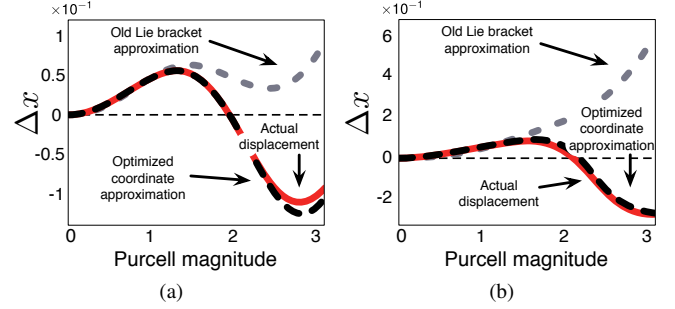
most efficient link length ratio [7]) does not even capture the approach of an optimal amplitude.

B. Optimal Stroke at Low Reynolds Number

Recognizing that the square Purcell stroke is not the most efficient choice for locomotion, Tam and Hosoi [7] investigated optimal stroke patterns. Their basic finding was that optimal gaits tend to be rounded oblongs; this makes sense from our CCF standpoint, as rounded curves have larger area-to-perimeter ratios than do curves with sharp angles, and the non-uniformity of the CCFs can be expected to bias the optimal curves away from simple circles.[17] A second, more striking, result was that the maximum-displacement-per-cycle stroke is pinched in at the center, rather than being convex. This "peanut shape" was presented as the result of direct optimization over the space of strokes parameterized by Fourier series, but with the aid of the CCFs, we can see *why* it was the result: by following the zero-contour of the x CCF (Fig. 8(a)), such strokes enclose as much negative area as possible, while avoiding positive areas that would reduce the magnitude of the total integral.

Note that in describing this optimal stroke, we are focusing only on strokes that form simple loops around the origin, and not including other optimizers, such as those that encircle the large positive regions in the corners of the plot as discussed in [34]. This focus derives from our interest in maximum displacement strokes as seeds in the search for maximum-efficiency strokes [11], [23]; as pointed out in [35], strokes in the corners are unlikely to be feasible for realistic systems, engender some ambiguity as to what makes up a single stroke cycle, and contain "unproductive" motions that reduce the overall efficiency.

C. Optimal Stroke at High Reynolds Number

Kanso [8] used a similar direct optimization approach to find good gaits for the high Reynolds number swimmer. While the set of candidate gaits was restricted to simple ellipses, limiting our ability to comment here on any commonalities between the

---

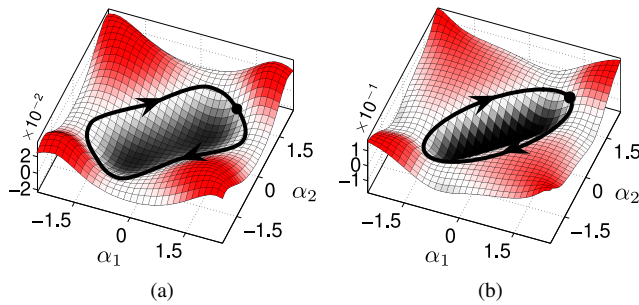[17]We examine the relationship between perimeter length and stroke effort in [23].

Fig. 8: Maximum-displacement strokes for low (a) and high (b) swimmers follow the zero-contours of their respective CCFs.

optimal stroke shape and CCF contours, the optimal ellipses were shown to have major axes aligned with the $\alpha_1 = \alpha_2$ direction in the shape space. As shown in Fig. 8(b), such ellipses closely approximate the zero contours of the x CCF, encircling the central well and avoiding the surrounding peaks.

VII. CONCLUSIONS

In this paper, we present a novel perspective for modeling articulated swimmers, which in turn improves upon existing methods for prescribing strokes. The connection vector fields, which we originally developed for mechanical systems, provide a concise visualization of the swimmers' dynamics. They naturally induce the constraint curvature functions, which geometrically capture the effect of oscillatory strokes. Our coordinate optimization approach makes these CCFs significantly more accurate than similar CCFs considered by others in the swimming community, especially when analyzing large-amplitude (and hence generally more efficient) strokes.

As extensions of the principles outlined here, we have demonstrated the usefulness of these tools in analyzing swimmers with a finite number of parameters controlling continuous deformation [23] and underactuated systems with elastic "shape" modes [36]. Our present work is examining the feasibility of using the CCFs to identify good regions of the stroke-function space in which to look for optimal strokes. We will also generate connection vector fields and CCFs for the hydrodynamically coupled swimming models, for comparison with the first-order models. Finally, we are in the process of generalizing our approach to include both visualization of the Lie bracket for more than two shape parameters and systems with fully three-dimensional translation and rotation.

ACKNOWLEDGMENT

REFERENCES

[1] G. Taylor, "Analysis of the swimming of microscopic organisms," *Proceedings of the Royal Society of London. Series A, Mathematical and Physical Sciences*, vol. 209, no. 29, pp. 447–461, 1951.

[2] E. M. Purcell, "Life at low Reynolds numbers," *American Journal of Physics*, vol. 45, no. 1, pp. 3–11, January 1977.

[3] G. V. Lauder and P. G. A. Madden, "Fish locomotion: Kinematics and hydrodynamics of flexible foil-like fins," *Experiments in Fluids*, vol. 43, pp. 641–653, July 2007.

[4] K. McIsaac and J. P. Ostrowski, "Motion planning for anguilliform locomotion," *Robotics and Automation*, pp. 637–652, Jan 2003. [Online]. Available: http://ieeexplore.ieee.org/xpls/abs_all.jsp?arnumber=1220714

[5] K. A. Morgansen, B. I. Triplett, and D. J. Klein, "Geometric methods for modeling and control of free-swimming fin-actuated underwater vehicles," *IEEE Transactions on Robotics*, vol. 23, no. 6, pp. 1184–1199, Jan 2007. [Online]. Available: http://ieeexplore.ieee.org/xpls/abs_all.jsp?arnumber=4399955

[6] S. D. Kelly, "The mechanics and control of driftless swimming," in press.

[7] D. Tam and A. E. Hosoi, "Optimal stroke patterns for Purcell's three-link swimmer," *Phys. Review Letters*, vol. 98, no. 6, p. 068105, 2007.

[8] E. Kanso, "Swimming due to transverse shape deformations," *Journal of Fluid Mechanics*, vol. 631, pp. 127–148, 2009.

[9] E. Kanso, J. E. Marsden, and J. B. Melli-Huber, "Locomotion of articulated bodies in a perfect fluid," *Journal of Nonlinear Science*, vol. 15, pp. 255–289, 2005.

[10] J. B. Melli, C. W. Rowley, and D. S. Rufat, "Motion planning for an articulated body in a perfect planar fluid," *SIAM Journal of Applied Dynamical Systems*, vol. 5, no. 4, pp. 650–669, November 2006.

[11] J. E. Avron and O. Raz, "A geometric theory of swimming: Purcell's swimmer and its symmetrized cousin," *New Journal of Physics*, vol. 9, no. 437, 2008.

[12] J. H. Hannay, "Swimming holonomy principles, exemplified with a euler fluid in two dimensions," *Journal of Physics A: Mathematical and Theoretical*, vol. 45, p. 065501, January 2012.

[13] R. M. Murray and S. S. Sastry, "Nonholonomic motion planning: Steering using sinusoids," *IEEE Transactions on Automatic Control*, vol. 38, no. 5, pp. 700–716, Jan 1993.

[14] S. D. K. Kelly and R. M. Murray, "Geometric phases and robotic locomotion," *J. Robotic Systems*, vol. 12, no. 6, pp. 417–431, Jan 1995.

[15] A. M. Bloch *et al.*, *Nonholonomic Mechanics and Control*. Springer, 2003.

[16] J. P. Ostrowski and J. Burdick, "The mechanics and control of undulatory locomotion," *International Journal of Robotics Research*, vol. 17, no. 7, pp. 683–701, July 1998.

[17] E. A. Shammas, H. Choset, and A. A. Rizzi, "Geometric motion planning analysis for two classes of underactuated mechanical systems," *Int. J. of Robotics Research*, vol. 26, no. 10, pp. 1043–1073, 2007.

[18] A. Shapere and F. Wilczek, "Geometry of self-propulsion at low Reynolds number," *Journal of Fluid Mechanics*, vol. 198, pp. 557–585, 1989.

[19] R. L. Hatton and H. Choset, "Connection vector fields for underactuated systems," in *Proceedings of the IEEE BioRobotics Conference*, October 2008, pp. 451–456.

[20] ——, "Approximating displacement with the body velocity integral," in *Proceedings of Robotics: Science and Systems V*, Seattle, WA USA, June 2009.

[21] ——, "Optimizing coordinate choice for locomoting systems," in *Proceedings of the IEEE International Conference on Robotics and Automation*, Anchorage, AK USA, May 2010, pp. 4493–4498.

[22] ——, "Connection vector fields and optimized coordinates for swimming systems at low and high Reynolds numbers," in *Proceedings of the ASME Dynamic Systems and Controls Conference (DSCC)*, Cambridge, Massachusetts, USA, Sep 2010.

[23] ——, "Kinematic cartography for locomotion at low Reynolds numbers," in *Proceedings of Robotics: Science and Systems VII*, Los Angeles, CA USA, June 2011.

[24] R. G. Cox, "The motion of long slender bodies in a viscous fluid part 1. general theory," *J. Fluid Mechanics*, vol. 44, no. 4, pp. 791–810, 1970.

[25] S. D. Kelly and R. M. Murray, "Modeling efficient pisciform swimming for control," *International Journal of Robust and Nonlinear Control*, vol. 10, no. 4, pp. 217–241, 2000.

[26] F. Boyer, M. Porez, A. Leroyer, and M. Visonneau, "Fast dynamics of an eel-like robot—comparisons with navier-stokes simulations," *IEEE Transactions on Robotics*, vol. 24, no. 6, pp. 1274–1288, December 2008.

[27] R. L. Hatton and H. Choset, "Geometric motion planning: The local connection, Stokes' theorem, and the importance of coordinate choice," *International Journal of Robotics Research*, vol. 30, no. 8, pp. 988–1014, July 2011.

[28] W. M. Boothby, *An Introduction to Differentiable Manifolds and Riemannian Geometry*. Academic Press, 1986.

[29] J. E. Radford and J. W. Burdick, "Local motion planning for nonholonomic control systems evolving on principal bundles," in *Proceedings of the International Symposium on Mathematical Theory of Networks and Systems*, Padova, Italy, 1998.

[30] R. L. Hatton and H. Choset, "Nonconservativity and noncommutativity in locomotion," *SIAM Journal of Applied Dynamical Systems*, (submitted).

[31] Q. Guo, M. K. Mandal, and M. Y. Li, "Efficient Hodge-Helmholtz decomposition of motion fields," *Pattern Recognition Letters*, vol. 26, no. 4, pp. 493–501, 2005.

[32] G. B. Arfken, *Mathematical Methods for Physicists*, 6th ed. Elsevier, 2005.

[33] L. Becker, S. A. Koehler, and H. A. Stone, "On self-propulsion of micro-machines at low Reynolds number: Purcell's three-link swimmer," *Journal of Fluid Mechanics*, vol. 490, pp. 15–35, 2003.

[34] O. Raz and J. E. Avron, "Comment on "optimal stroke patterns for purcell's three-link swimmer"," *Physical Review Letters*, vol. 100, p. 029801, January 2008.

[35] D. Tam and A. E. Hosoi, "Tam and hosoi reply:," *Phys. Rev. Lett.*, vol. 100, no. 2, p. 029802, Jan 2008.

[36] L. J. Burton, R. L. Hatton, H. Choset, and A. E. Hosoi, "Two-link swimming using buoyant orientation," *Physics of Fluids*, vol. 22, p. 091703, September 2010.

Ross L. Hatton is an Assistant Professor of Mechanical Engineering at Oregon State University. He received PhD and MS degrees in Mechanical Engineering from Carnegie Mellon University, following an SB in the same from Massachusetts Institute of Technology. His research focuses on understanding the fundamental mechanics of locomotion, making advances in mathematical theory accessible to an engineering audience, and on finding abstractions that facilitate human control of unconventional locomotors.

Howie Choset is a Professor of Robotics at Carnegie Mellon University. Motivated by applications in confined spaces, Choset has created a comprehensive program in snake robots, which has led to basic research in mechanism design, path planning, motion planning, and estimation. Professor Choset's students have won best paper awards at the RIA, 1999 and ICRA in 2003, and ASME DSCC in 2010; his group's work has been nominated for best papers at ICRA in 1997, IROS in 2003 and 2007, and CLAWAR in 2012 (best biorobotics paper, best student paper); won best paper at IEEE Bio Rob in 2006; won best video at ICRA 2011; and was nominated for best video in ICRA 2012. In 2002 the MIT Technology Review elected Choset as one of its top 100 innovators in the world under 35. In 2005, MIT Press published a textbook, lead authored by Choset, entitled "Principles of Robot Motion." Recently, Choset co-founded a company called Medrobotics (formerly Cardiorobotics) which makes a small surgical snake robot for minimally invasive surgery.